

Identification of interstellar cyanamide towards the hot molecular core G358.93–0.03 MM1

Arijit Manna¹ • Sabyasachi Pal¹

Abstract The amide-related molecules are essential for the formation of the other complex bio-molecules and an understanding of the prebiotic chemistry in the interstellar medium (ISM). We presented the first detection of the rotational emission lines of the amide-like molecule cyanamide (NH_2CN) towards the hot molecular core G358.93–0.03 MM1 using the Atacama Large Millimeter/Submillimeter Array (ALMA). Using the rotational diagram model, the derived column density of NH_2CN towards the G358.93–0.03 MM1 was $(5.9 \pm 2.5) \times 10^{14} \text{ cm}^{-2}$ with a rotational temperature of $100.6 \pm 30.4 \text{ K}$. The derived fractional abundance of NH_2CN towards the G358.93–0.03 MM1 with respect to H_2 was $(4.72 \pm 2.0) \times 10^{-10}$, which is very similar to the existent three-phase warm-up chemical model abundances of NH_2CN . We compare the estimated abundance of NH_2CN towards G358.93–0.03 MM1 with other sources, and we observe the abundance of NH_2CN towards G358.93–0.03 MM1 is nearly similar to that of the sculptor galaxy NGC 253 and the low-mass protostars IRAS 16293–2422 B and NGC 1333 IRAS4A2. We also discussed the possible formation mechanisms of NH_2CN towards the hot molecular cores and hot corinos, and we find that the NH_2CN molecule was created in the grain-surfaces of G358.93–0.03 MM1 via the neutral-neutral reaction between NH_2 and CN .

Keywords ISM: individual objects (G358.93–0.03 MM1) – ISM: abundances – ISM: kinematics and dynamics – stars: formation – astrochemistry

Arijit Manna
Sabyasachi Pal

¹Department of Physics and Astronomy, Midnapore City College, Paschim Medinipur, West Bengal, India 721129
email: arijitmanna@mconline.org.in

1 Introduction

The amide-type molecule cyanamide (NH_2CN) was formed with amide and cyanide functional groups, which acted as a possible precursor of urea (NH_2CONH_2) in the ISM. The urea was formed via the hydrolysis of NH_2CN in the ISM (Kilpatrick 1947). The carbodiimide (HNCNH) molecule is known as one of the isomer of NH_2CN , which contains the $-\text{NCN}-$ frame (Turner et al. 1975; Coutens et al. 2018). The molecules with the $-\text{NCN}-$ frame play a major role in linking biological processes and in the assembly of amino acids into peptides (Williams & Ibrahim 1981). The HNCNH molecule forms due to photochemical and thermally induced reactions of NH_2CN in interstellar ice analogues (Duvernay et al. 2005). Except for urea, the NH_2CN molecule also acts as a possible precursor of 2-amino-oxazole, cytosine, 3'-cyclic phosphate (pyrimidine ribonucleotide), and beta-ribocytidine-2 via biochemistry synthesis routes towards the hot cores/corinos (Jiménez-Serra et al. 2020). The NH_2CN molecule contains 0^+ and 0^- substates with a pyramidal equilibrium structure (Sharma 2021). The dipole moments of the 0^+ and 0^- substrates are $\mu_a = 4.25 \pm 0.02 \text{ D}$ and $\mu_a = 4.24 \pm 0.02 \text{ D}$, respectively (Brown et al. 1985; Sharma 2021). In the ISM, evidence of NH_2CN was found towards the hot molecular cores Sgr B2 (N), Orion KL, IRAS 20126+410, and NGC 6334I (Turner et al. 1975; White et al. 2003; Palau et al. 2017; Ligterink et al. 2020). The rotational emission lines of NH_2CN were also detected towards the low-mass solar-like protostars IRAS 16293–2422 B and NGC 1333 IRAS2A using the ALMA and Plateau de Bure Interferometer (PdBI) (Coutens et al. 2018). Outside of the Milky Way, evidence of the NH_2CN molecule was also found towards the sculptor galaxy NGC 253 and the starburst galaxy M82 (Martín et al. 2006; Aladro et al. 2011). Recently, the emission lines of NH_2CN were also detected towards the hot molecular core G10.47+0.03 using the ALMA band 4, with an estimated column density of $6.60 \times 10^{15} \text{ cm}^{-2}$ and a rotational temperature of 201.2 K (Manna & Pal 2022a).

Table 1 Observation summary of G358.93–0.03 using the ALMA band 6.

Band	Date of observation (YYYY MMM DD)	Start time (hh:mm)	End time (hh:mm)	Number of antennas	Frequency range (GHz)	Spectral resolution (kHz)	Field of View (FOV) (′′)
6	2019 Oct 07	22:01	22:23	42	216.44–217.38 218.08–218.55 219.88–220.35 220.33–220.80	488.28 282.23 282.23 282.23	26.599

The search for complex organic molecules using the millimeter and submillimeter telescopes in the star-formation regions gives us an idea about the chemistry in the ISM. The hot molecular cores are one of the highly chemically rich phases that are located in the high-mass star-formation regions, and they play an important role in increasing the chemical complexity in the ISM (Shimonishi et al. 2021). The hot molecular cores are the ideal astronomical objects in the ISM to study the different complex and prebiotic molecular lines because they have a warm temperature (≥ 100 K), a high gas density ($n_{\text{H}_2} \geq 10^6 \text{ cm}^{-3}$), and a small source size (≤ 0.1 pc) (van Dishoeck & Blake 1998). The chemistry of the hot core is characterised by the sublimation of ice mantles, which accumulate during the star-formation activities (Shimonishi et al. 2021). The gaseous molecules and atoms are frozen onto the dust grains of cold molecular clouds and prestellar cores. When the temperature increases due to star-formation activities, the chemical interaction between heavy compounds becomes active on the grain surfaces, and the complex organic molecules are formed in the star-formation regions (Garrod & Herbst 2006; Garrod 2013; Shimonishi et al. 2021). So, the highly dense, warm, and chemically rich abundant molecules around the protostars produce the strongest molecular line emitters, known as the hot molecular cores (Shimonishi et al. 2021). The period of the hot molecular cores is thought to last about 10^5 years (medium warm-up phase) to 10^6 years (slow warm-up phase) (van Dishoeck & Blake 1998; Garrod & Herbst 2006; Garrod 2013).

The hot molecular core G358.93–0.03 MM1 is located in the high-mass star-formation region G358.93–0.03. The high-mass star-formation region G358.93–0.03 is located at a distance of $6.75^{+0.37}_{-0.68}$ kpc from the earth (Reid et al. 2014; Brogan et al. 2019). The luminosity of the high-mass star-formation region G358.93–0.03 was $\sim 7.660 \times 10^3 L_{\odot}$ with total gas mass $167 \pm 12 M_{\odot}$ (Brogan et al. 2019). The high-mass star-formation region G358.93–0.03 has eight submillimeter wavelength continuum sources, i.e., G358.93–0.03 MM1 to G358.93–0.03 MM8. Among the eight sources, G358.93–0.03 MM1 and G358.93–0.03 MM3 emit the molecular line emission (Brogan et al. 2019). That means G358.93–0.03 MM1 and G358.93–0.03 MM3 are hot molecular cores because those two sources emit both continuum and line emission (Brogan et al. 2019; Bayandina et al. 2022). Earlier, Brogan et al. (2019) claimed that

G358.93–0.03 MM1 is more chemically rich than G358.93–0.03 MM3. Earlier, the maser lines of methanol (CH_3OH), durated water (HDO), and isocyanic acid (HNCO) were detected towards the G358.93–0.03 MM1 using the ALMA, TMRT, and VLA radio telescopes (Brogan et al. 2019; Chen et al. 2020). The emission lines of methyl cyanide (CH_3CN) were also detected towards the G358.93–0.03 MM1 and the G358.93–0.03 MM3 using the ALMA (Brogan et al. 2019).

In this article, we present the first detection of the rotational emission lines of NH_2CN towards the hot molecular core region G358.93–0.03 MM1 using the ALMA band 6. The ALMA observations and data reduction of the high-mass star-formation region G358.93–0.03 were presented in Section 2. The result of the detection of emission lines of NH_2CN towards the G358.93–0.03 MM1 was shown in Section 3. The discussion and conclusion of the detection of NH_2CN towards the G358.93–0.03 MM1 were shown in Section 4 and 5.

2 Observations and data reduction

The high-mass star-formation region G358.93–0.03 was observed using the Atacama Large Millimeter/Submillimeter Array (ALMA) band 6 (frequency range of 216.44–220.80 GHz) receiver to study the massive protostellar accretion outburst (ID: 2019.1.00768.S., PI: Crystal Brogan). The observations were conducted on October 7th, 2019 with on-source integration times of 604.80 sec. The phase centre of G358.93–0.03 was $(\alpha, \delta)_{\text{J2000}} = 17:43:10.000, -29:51:46.000$. The observation was carried out using the forty-two antennas, with a minimum baseline of 15 m and a maximum baseline of 783 m. During the observation, J1744–3116 was used as a phase calibrator, and J1924–2914 was used as a flux calibrator and bandpass calibrator. The observation details are shown in Table 1.

We used the Common Astronomy Software Application (CASA 5.4.1) for the reduction of data using the ALMA data analysis pipeline (McMullin et al. 2007). For flux calibration, we applied the CASA task SETJY using the Perley-Butler 2017 flux calibrator model (Perley & Butler 2017). For bandpass calibration and flagging the band antenna data, we applied the CASA pipeline tasks `hi_fa_bandpassflag`

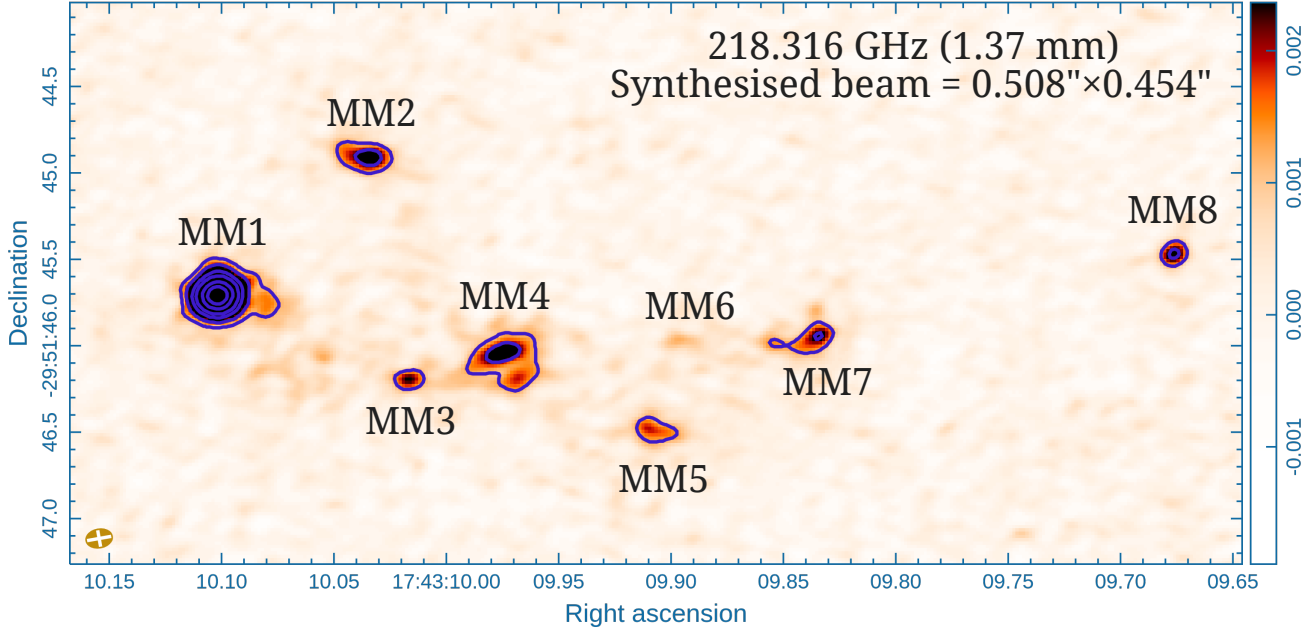


Fig. 1 Sub-millimeter wavelength (1.37 mm) continuum emission image of high-mass star-formation region G358.93–0.03. The angular resolution of the continuum image was $0.508'' \times 0.454''$. In the image, MM1 to MM8 are the sub-millimeter continuum sources situated in the massive star-formation region G358.93–0.03. The contour (blue colour) levels started at 3σ where $\sigma = 16.40 \mu\text{Jy}$ is the RMS of the continuum emission image, and the contour level increased by a factor of $\sqrt{2}$. The bandwidth of the image was 0.47 GHz.

and `hifa_flagdata`. After the flux calibration, band-pass calibration, and flagging of the bad channels, we employed the task `MSTRANSFORM` to separate the target object G358.93–0.03 with all available rest frequencies. We created four continuum emission images of G358.93–0.03 using the CASA task `TCLEAN` with the `HOGBOM` deconvolver using the frequency ranges of 216.44–217.38 GHz, 218.08–218.55 GHz, 219.88–220.35 GHz, and 220.33–220.80 GHz, respectively. Among the four individual continuum emission images, we have shown the sub-millimeter wavelength continuum emission map of the high-mass star-formation region G358.93–0.03 at frequency 218.316 GHz (1.37 mm) in Figure 1 as an example. The continuum emission image of G358.93–0.03 was created using the Cube Analysis and Rendering Tool for Astronomy (CARTA) software package (Comrie et al. 2021). The bandwidth of this continuum emission image of G358.93–0.03 at frequency 218.316 GHz is 0.47 GHz. The effect of bandwidth smearing in those observed frequency ranges is minimal as according to Mangum (2020) the maximum bandwidth to avoid amplitude smearing between the frequency ranges of 216.44 GHz and 220.80 GHz is ~ 1.2 GHz. From the continuum emission map of G358.93–0.03 at frequency 218.316 GHz, we identified the eight sub-millimeter wavelength continuum sources, G358.93–0.03 MM1 to G358.93–0.03 MM8. Among the eight sources, G358.93–0.03 MM1 and G358.93–0.03 MM3 are hot molecular cores because both sources emit the line emission as well as the emission lines of CH_3CN (Bro-

gan et al. 2019). Earlier, Brogan et al. (2019) showed the first sub-millimeter continuum emission map of G358.93–0.03, but the authors were unable to clearly identify the continuum sources G358.93–0.03 MM6 and G358.93–0.03 MM8 due to the lower image resolution. We first individually detected all eight sub-millimeter wavelength continuum sources in the massive star-formation region G358.93–0.03 using the ALMA at wavelength 1.37 mm with an angular resolution of $0.508'' \times 0.454''$. After the continuum analysis, we employed the task `UVCONTSUB` to subtract the background continuum emission from the UV plane of the calibrated data. Now we created the spectral images at frequency ranges of 216.44–217.38 GHz, 218.08–218.55 GHz, 219.88–220.35 GHz, and 220.33–220.80 GHz using the task `TCLEAN` with the `SPECMODE = CUBE` parameter. Finally, we used the CASA task `IMPBCOR` for the correction of the synthesised beam pattern in the continuum and spectral images of G358.93–0.03.

3 Results

3.1 Sub-millimeter wavelength continuum emission towards the G358.93–0.03 MM1

Among the eight sub-millimeter wavelength continuum sources, we mainly focus on the G358.93–0.03 MM1 ($\alpha, \delta_{J2000} = 17:43:10.102, -29:51:45.714$) because that

Table 2 Summary of the continuum image of G358.93–0.03 MM1.

Frequency (GHz)	Wavelength (mm)	Integrated Flux (mJy)	Peak flux (mJy beam ⁻¹)	Beam size ("×")	RMS (μJy)	Position angle (°)
216.90	1.38	61.72±3.7	50.60±1.9	0.507×0.456	22.12	88.879
218.31	1.37	72.31±3.8	56.83±1.8	0.508×0.454	16.40	87.515
220.11	1.36	72.12±3.5	61.35±2.0	0.497×0.455	28.23	89.169
220.56	1.35	77.91±4.2	69.42±2.2	0.494×0.454	22.22	86.827

source is the brightest sub-millimeter wavelength continuum source in the massive star-formation region G358.93–0.03, which hosts the line-rich hot core (Brogan et al. 2019; Bayandina et al. 2022). We presented the sub-millimeter wavelength continuum emission images of the G358.93–0.03 MM1 at frequencies of 216.90 GHz (1.38 mm), 218.31 GHz (1.37 mm), 220.11 GHz (1.36 mm), and 220.56 GHz (1.35 mm) in Figure 2. Now we used the CASA task IMFIT to fit the 2D Gaussian over all the continuum images and obtained an integrated flux density, peak flux density, synthesised beam size, position angle, and RMS, which are presented in Table 2. We notice that the hot molecular core G358.93–0.03 MM1 was resolved in ALMA band 6 as it was found that the source was larger than the synthesised beam size. Earlier, Brogan et al. (2019) also detected the millimeter-wavelength continuum emission from the eight individual continuum sources (G358.93–0.03 MM1 to G358.93–0.03 MM8) of G358.93–0.03 at frequencies of 195.58 GHz, 233.75 GHz, and 337.26 GHz, and the author mentioned the continuum emission maps of the eight individual continuum sources were resolved within the observable frequency ranges.

3.2 Estimation of hydrogen (H₂) column density and dust optical depth (τ_v) towards the G358.93–0.03 MM1

The peak flux density (S_v) of optically thin dust continuum emission can be expressed as,

$$S_v = B_v(T_d)\tau_v\Omega_{beam} \quad (1)$$

where τ_v presented the optical depth, B_v(T_d) indicated the Planck function at dust temperature T_d (Whittet 1992), and Ω_{beam} = (π/4 ln 2) × θ_{major} × θ_{minor} is the solid angle of the synthesised beam. The expression of optical depth in terms of the mass density of dust can be written as,

$$\tau_v = \rho_d\kappa_vL \quad (2)$$

where κ_v is the mass absorption coefficient, L is the path length, and ρ_d indicates the mass density of dust. The mass

density of the dust can be expressed in terms of the dust-to-gas mass ratio (Z).

$$\rho_d = Z\mu_H\rho_{H_2} = Z\mu_H N_{H_2} 2m_H/L \quad (3)$$

where ρ_{H₂} is the hydrogen mass density, μ_H presented the mean atomic mass per hydrogen, m_H indicated the mass of hydrogen, and N_{H₂} is the column density of hydrogen. We take the dust temperature T_d to be 150 K (Chen et al. 2020), μ_H = 1.41, and Z = 0.01 (Cox & Pilachowski 2000). The estimated peak flux density of the dust continuum of the G358.93–0.03 MM1 at different frequencies is presented in Table 2. From equations 1, 2, and 3, the column density of molecular hydrogen can be expressed as,

$$N_{H_2} = \frac{S_v/\Omega}{2\kappa_v B_v(T_d)Z\mu_H m_H} \quad (4)$$

During the estimation of the mass absorption coefficient (κ_v), we adopted the formula κ_v = 0.90(ν/230GHz)^β cm² g⁻¹ (Motogi et al. 2019), where k₂₃₀ = 0.90 cm² g⁻¹ indicated the emissivity of the dust grains at a gas density of 10⁶ cm⁻³, which covered by a thin ice mantle at 230 GHz. We used the dust spectral index β ~ 1.7 (Brogan et al. 2019). Using the mass absorption coefficient formula, we estimated the value of κ_v to be 0.814, 0.823, 0.835, and 0.838 for frequencies of 216.90, 218.31, 220.11, and 220.56 GHz, respectively. We estimated the column density of hydrogen (N_{H₂}) for the four frequency regions towards the G358.93–0.03 MM1, which was presented in Table 3. We take the average value to estimate the resultant hydrogen column density towards the G358.93–0.03 MM1. The estimated column density of hydrogen towards the G358.93–0.03 MM1 was (1.25±0.11)×10²⁴ cm⁻². We also determine the value of optical depth (τ_v) using the following equation,

$$T_{mb} = T_d(1 - \exp(-\tau_v)) \quad (5)$$

where T_{mb} is the brightness temperature and T_d is the dust temperature of G358.93–0.03 MM1. For estimation of the brightness temperature, we used the Rayleigh-Jeans approximation, 1 Jy beam⁻¹ ≡ 118 K (Gorai et al. 2021). The calculated dust optical depth of G358.93–0.03 MM1 with

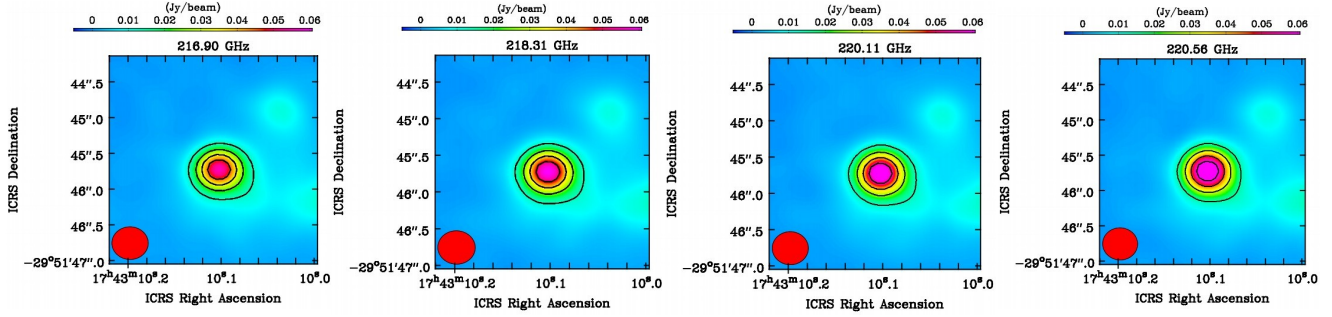


Fig. 2 Sub-millimeter continuum images of G358.93–0.03 MM1 obtained with ALMA band 6 at frequencies of 216.90 GHz ($\sigma = 22.12 \mu\text{Jy beam}^{-1}$), 218.31 GHz ($\sigma = 16.40 \mu\text{Jy beam}^{-1}$), 220.11 GHz ($\sigma = 28.23 \mu\text{Jy beam}^{-1}$), and 220.56 GHz ($\sigma = 22.22 \mu\text{Jy beam}^{-1}$). The contour level started at 3σ , where σ is the RMS of each continuum image, and the contour level increased by a factor of $\sqrt{2}$. The red circles indicate the synthesised beam of the continuum images.

individual frequencies was presented in Table 3. The average dust optical depth was 0.0475. The estimated dust optical depth indicated that the G358.93–0.03 MM1 is optically thin between the frequency ranges of 216.44–220.80 GHz.

3.3 Identification of the NH_2CN towards the G358.93–0.03 MM1

After the production of the spectral images of G358.9–0.03 from the observable frequency ranges, we see that only the spectra of G358.93–0.03 MM1 and G358.93–0.03 MM3 show any line emission. We did not observe any line emission from other sources in G358.93–0.03. We focus to study of the complex organic molecules on the G358.93–0.03 MM1 rather than the G358.93–0.03 MM3 because the G358.93–0.03 MM1 is more chemically rich than the G358.93–0.03 MM3. We extracted the sub-millimeter wavelength molecular rich spectra from the spectral images of G358.93–0.03 to create a $0.781''$ diameter circular region over the hot molecular core G358.93–0.03 MM1 ($\alpha, \delta_{J2000} = 17:43:10.102, -29:51:45.714$). The systematic velocity of G358.93–0.03 MM1 was -16.5 km s^{-1} (Brogan et al. 2019). We used the CASSIS (Vastel et al. 2015) with the Line Analysis module to examine the molecular emission lines from the sub-millimeter spectra of G358.93–0.03 MM1. After the spectral analysis, we identified the rotational emission lines of amide-like molecules NH_2CN from

Table 3 Column density of hydrogen and optical depth towards G358.93–0.03 MM1.

Wavelength (mm)	Hydrogen column density (cm^{-2})	Optical depth (τ_ν)
1.38	$(1.28 \pm 0.10) \times 10^{24}$	0.0397
1.37	$(1.19 \pm 0.30) \times 10^{24}$	0.0457
1.36	$(1.32 \pm 0.20) \times 10^{24}$	0.0502
1.35	$(1.20 \pm 0.20) \times 10^{24}$	0.0561
Average Value	$(1.25 \pm 0.11) \times 10^{24}$	0.0475

the sub-millimeter spectra G358.93–0.03 MM1 using the Jet Population Laboratory (JPL) (Pickett et al. 1998) spectroscopic database. We detected the seven rotational emission lines of NH_2CN at frequencies ranging from 216.44 to 220.80 GHz. There are no missing transition lines of NH_2CN within the observable frequency ranges as per the JPL molecular database.

After the identification, we fitted the Gaussian model over the detected rotational emission spectra of NH_2CN using the Levenberg-Marquardt algorithm, which was available in CASSIS. After fitting a Gaussian model over the detected spectra of NH_2CN , we obtained molecular transitions ($J'_{K'_a, K'_c} - J''_{K''_a, K''_c}$), upper state energy (E_u) in K, line intensity ($S\mu^2$) in Debye², FWHM in km s^{-1} , Einstein coefficients (A_{ij}) in s^{-1} , peak intensity in K, and integrated intensity ($\int T_{\text{mb}} dV$) in K km s^{-1} . After the spectral analysis, we noticed $J = 11(1,11) - 10(1,10) V = 1$, $J = 11(2,10) - 10(2,9) V = 0$, $J = 11(0,11) - 10(0,10) V = 0$, $J = 11(2,9) - 10(2,8) V = 0$, $J = 11(3,9) - 10(3,8) V = 0$, and $J = 11(3,8) - 10(3,7) V = 0$ transition lines of NH_2CN are not contaminated with other nearby molecular transitions. We also observed that the $J = 11(1,11) - 10(1,10) V = 0$ transition line of NH_2CN is blended with the NH_2CHO molecular transition. During the spectral analysis, we notice the $J = 11(3,9) - 10(3,8) V = 0$, and $J = 11(3,8) - 10(3,7) V = 0$ transition lines of NH_2CN are present in a single spectral profile, which indicates the current spectral resolution is insufficient to resolve those two transition lines of NH_2CN towards the G358.93–0.03 MM1. The Gaussian-fitting rotational emission spectra of NH_2CN were shown in Figure 3 and a summary of the Gaussian-fitting spectral line properties of NH_2CN was presented in Table 4.

3.4 Spatial distribution of NH_2CN towards the G358.93–0.03 MM1

We created the integrated emission maps of the non-blended transitions of NH_2CN towards the G358.93–0.03 MM1 using the CASA task IMMOMENTS. During the run of the task

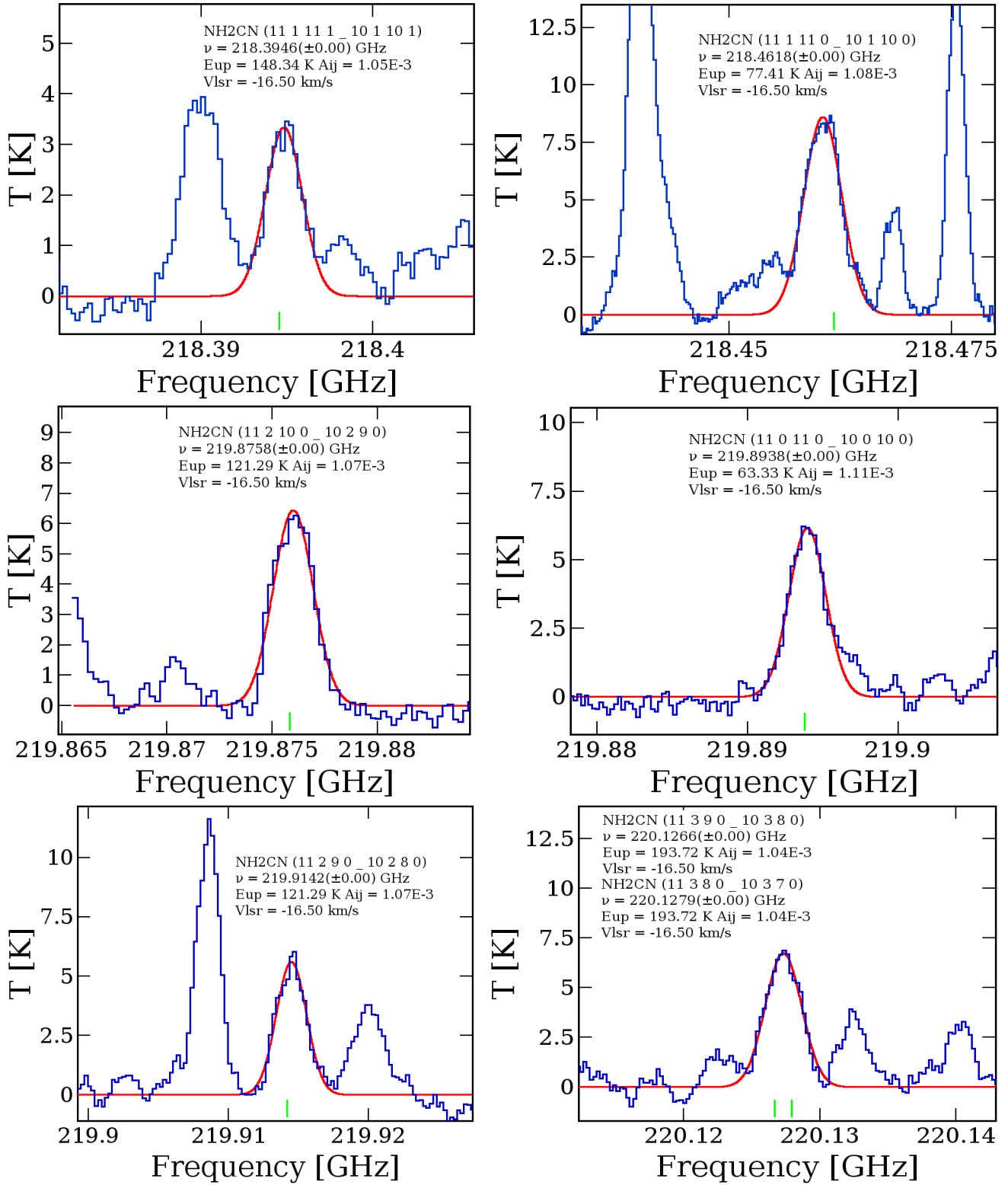


Fig. 3 Rotational emission spectra of NH₂CN towards the G358.93–0.03 MM1 with different molecular transitions. The blue spectrum indicated the detected sub-millimeter spectrum of G358.93–0.03 MM1, and the red synthetic spectra indicated the Gaussian model that fitted over the detected emission lines of NH₂CN. The green vertical lines represented the rest frequency positions of the identified transitions of NH₂CN.

Table 4 Summary of the Gaussian fitting line properties of the NH₂CN towards the hot molecular core G358.93–0.03 MM1.

Observed frequency (GHz)	Transition ($J'_{K'_a K'_c} - J''_{K''_a K''_c}$)	E_u (K)	A_{ij} (s ⁻¹)	Peak intensity (K)	$S\mu^2$ (Debye ²) [†]	FWHM (km s ⁻¹)	V_{LSR} (km s ⁻¹)	$\int T_{mb}dV$ (K km s ⁻¹)	Remark
218.394	11(1,11)–10(1,10), V = 1	148.33	1.05×10^{-3}	3.459	199.330	3.358 ± 0.18	-16.51 ± 0.21	10.457 ± 1.21	Non blended
218.461	11(1,11)–10(1,10), V = 0	77.40	1.08×10^{-3}	8.663	612.666	8.310 ± 0.35	-16.50 ± 0.12	47.415 ± 0.22	Blended with NH ₂ CHO
219.875	11(2,10)–10(2,9), V = 0	121.29	1.07×10^{-3}	6.266	198.970	3.534 ± 0.13	-16.49 ± 0.94	18.059 ± 0.22	Non blended
219.893	11(0,11)–10(0,10), V = 0	63.32	1.11×10^{-3}	6.228	205.927	3.696 ± 0.28	-16.51 ± 0.82	18.732 ± 0.11	Non blended
219.914	11(2,9)–10(2,8), V = 0	121.29	1.07×10^{-3}	6.025	198.996	3.728 ± 0.25	-16.52 ± 0.23	17.249 ± 0.51	Non blended
220.126	11(3,9)–10(3,8), V = 0	193.72	1.04×10^{-3}	6.861	579.630	4.508 ± 0.17	-16.52 ± 0.29	28.392 ± 0.26	Non blended
220.127	11(3,8)–10(3,7), V = 0	193.72	10.4×10^{-3}	6.861	579.624	4.506 ± 0.36	-16.49 ± 0.17	28.389 ± 0.29	Non blended

[†]–The values of the $S\mu^2$ were taken from the JPL molecular database (Pickett et al. 1998).

IMMOMENTS, we specified the channel ranges of the spectral images where the emission lines of NH₂CN were identified. The resultant integrated emission maps of the NH₂CN towards the G358.93–0.03 MM1 were shown in Figure 4, which was overlaid on the 1.37 mm continuum emission map. We observed that the integrated NH₂CN emission maps show a peak at the position of continuum emission. The integrated emission maps indicated that the rotational emission lines of NH₂CN mainly come from the highly dense, warm inner hot core region of the G358.93–0.03 MM1. Now we used the CASA task IMFIT for fitting the 2D Gaussian over the integrated emission maps of NH₂CN to estimate the emitting regions of NH₂CN. The deconvolved synthesised beam sizes of the NH₂CN emitting regions were derived by the following equation:

$$\theta_S = \sqrt{\theta_{50}^2 - \theta_{beam}^2} \quad (6)$$

where θ_{beam} was the half-power width of the synthesised beam of the integrated emission maps and $\theta_{50} = 2\sqrt{A/\pi}$ presented the diameter of the circle whose area was surrounding the 50% line peak of NH₂CN (Manna & Pal 2022a,b). The derived emitting regions of NH₂CN are presented in Table 5. The emitting regions of NH₂CN were found to be in the range of 0.496''–0.513''. We observed that the derived NH₂CN emitting regions are comparable to or slightly greater than the synthesised beam sizes of the integrated emission maps. That indicates the transitions of NH₂CN were not well resolved spatially or, at best, marginally resolved towards the G358.93–0.03 MM1. So it is not possible to present any conclusions about the morphology of the spatial distribution of NH₂CN towards the G358.93–0.03 MM1. High-sensitivity data with higher spatial and angular resolution observations are required to understand the spatial distribution of NH₂CN towards the hot molecular core G358.93–0.03 MM1.

3.5 Rotational diagram analysis of NH₂CN

In this work, we have identified the seven rotational emission lines of NH₂CN towards the G358.93–0.03 MM1. Ro-

tational diagram analysis is the most efficient way to estimate the rotational temperature (T_{rot}) in K and the column density (N) in cm⁻² of the detected emission lines of NH₂CN. We used the rotational diagram model since we assumed that the observed rotational emission lines of NH₂CN are optically thin and that they are populated in local thermodynamic equilibrium (LTE) conditions. The LTE assumption was appropriate for the G358.93–0.03 MM1 because the gas density of the warm inner region of the hot core was $\sim 2 \times 10^7$ cm⁻³ (Stecklum et al. 2021). The equation of column density of the optically thin molecular emission lines can be expressed as (Goldsmith & Langer 1999),

$$N_u^{thin} = \frac{3g_u k_B \int T_{mb} dV}{8\pi^3 \nu S \mu^2} \quad (7)$$

where μ indicates the dipole moments of the NH₂CN, ν is the rest frequency, S indicates the line strength, g_u is the degeneracy of the upper state, $\int T_{mb} dV$ indicates the integrated intensity of the detected emission lines of the NH₂CN, and k_B is the Boltzmann constant. The total column density of NH₂CN under the LTE condition can be expressed as,

$$\frac{N_u^{thin}}{g_u} = \frac{N_{total}}{Q(T_{rot})} \exp(-E_u/k_B T_{rot}) \quad (8)$$

where, E_u is the upper-state energy of NH₂CN, T_{rot} is the rotational temperature of NH₂CN, and $Q(T_{rot})$ indicates the partition function of rotational temperature (T_{rot}). The partition function of NH₂CN at 75 K, 150 K, and 300 K is

Table 5 The emitting regions of non-blended transitions of NH₂CN towards the G358.93–0.03 MM1.

Transition [$J'_{K'_a K'_c} - J''_{K''_a K''_c}$]	Frequency [GHz]	E_{up} [K]	Emitting region [']
11(1,11)–10(1,10), V = 1	218.394	148.33	0.501
11(2,10)–10(2,9), V = 0	219.875	121.29	0.496
11(0,11)–10(0,10), V = 0	219.893	63.32	0.512
11(2,9)–10(2,8), V = 0	219.914	121.29	0.498
11(3,9)–10(3,8), V = 0	220.126	193.72	0.513
11(3,8)–10(3,7), V = 0	220.127	193.72	0.513

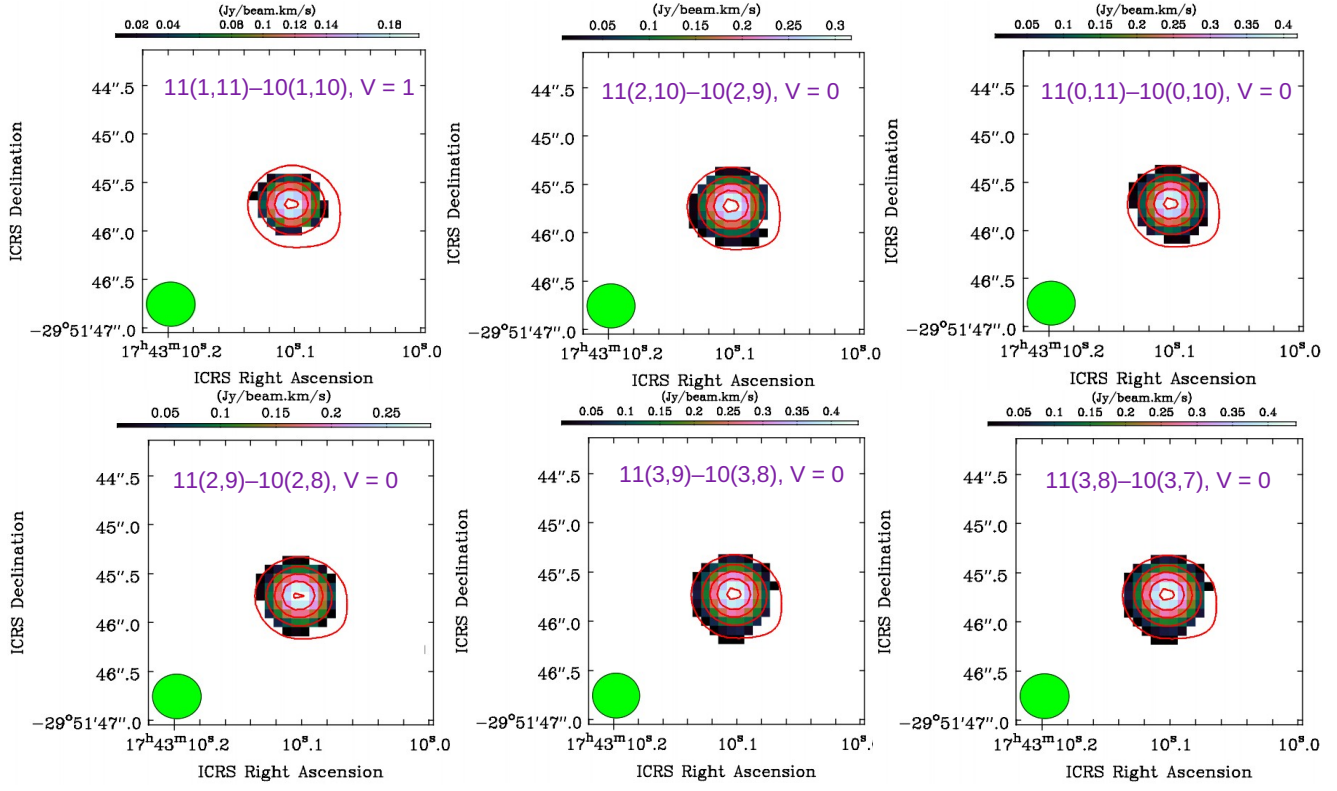


Fig. 4 Integrated emission maps of NH_2CN towards the G358.93–0.03 MM1. The emission maps were overlaid with the 1.37 mm continuum emission map (red contour). The contour levels are at 20%, 40%, 60%, 80%, and 100% of the continuum peak flux. The green circle indicated the synthesised beam of the integrated emission maps.

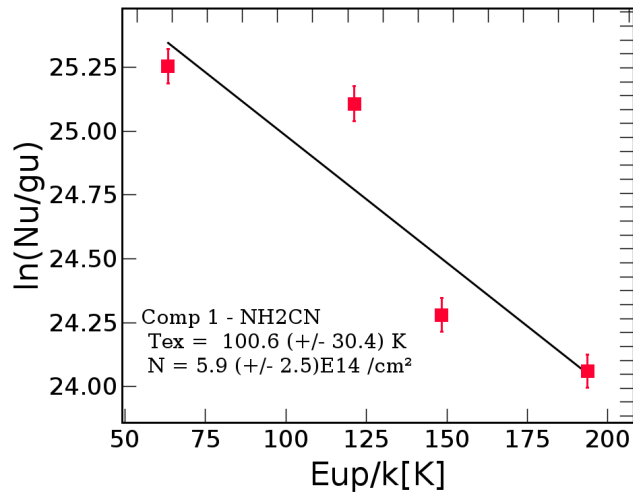


Fig. 5 Rotational diagram of NH_2CN towards the G358.93–0.03 MM1. The red-filled squares indicated the values of $\ln(N_u/g_u)$ which vary with different upper-state energies (E_u) of NH_2CN . The derived rotational temperature and column density of NH_2CN are mentioned in the figure.

1730.290, 5730.062, and 17902.30, respectively. Equation 8 can be rearranged as,

$$\ln\left(\frac{N_u^{thin}}{g_u}\right) = \ln(N) - \ln(Q(T_{rot})) - \left(\frac{E_u}{k_B T_{rot}}\right) \quad (9)$$

The equation 9 presents a linear relation between $\ln(N_u/g_u)$ and upper-state energy (E_u). After the estimation of $\ln(N_u/g_u)$ from equation 7, we fit a straight line to the estimated values of $\ln(N_u/g_u)$, which vary with E_u . After fitting the straight line, the rotational temperature was estimated from the inverse of the slope, and the column density was estimated from the intercept of the slope. For rotational diagram analysis, the spectral line parameters of NH_2CN are estimated by fitting a Gaussian model over the observed emission lines of NH_2CN , which were presented in Table 4. After spectral analysis, we notice only the $J = 11(1,11) - 10(1,10) V = 0$ transition line of NH_2CN is blended with NH_2CHO , and that transition was excluded from the rotational diagram analysis. We observed that $J = 11(2,10) - 10(2,9) V = 0$ and $J = 11(2,9) - 10(2,8) V = 0$ transitions have the same upper-state energy of 121.29 K. During the rotational diagram, we used the $J = 11(2,9) - 10(2,8) V = 0$ transition line because the line intensity of the $J = 11(2,9) - 10(2,8) V = 0$ transition line is slightly higher than that of the $J = 11(2,10) - 10(2,9) V = 0$ transition line. Similarly, we also observed that the $J = 11(3,9) - 10(3,8) V = 0$ and $J = 11(3,8) - 10(3,7) V = 0$ transitions of NH_2CN are present in the single spectral profile, and the upper-state energy of those two transitions is the same (193.72 K). So, we take the $J = 11(3,9) - 10(3,8) V = 0$ transition line for the rotational diagram because the line intensity of $J = 11(3,9) - 10(3,8) V = 0$ is slightly higher than the $J = 11(3,8) - 10(3,7) V = 0$ transition line. The rotational diagram analysis was carried out using the $J = 11(1,11) - 10(1,10) V = 1$, $J = 11(0,11) - 10(0,10) V = 0$, $J = 11(2,9) - 10(2,8) V = 0$, and $J = 11(3,9) - 10(3,8) V = 0$ transition lines of NH_2CN . The resultant rotational diagram of NH_2CN , which was computed using the ROTATIONAL DIAGRAM module in CASSIS, is shown in Figure 5. In the rotational diagram, the vertical red error bars represent the absolute uncertainty of $\ln(N_u/g_u)$, which was calculated from the $\int T_{mb} dV$ of the emission spectra. From the rotational diagram, the estimated column density of NH_2CN was $(5.9 \pm 2.5) \times 10^{14} \text{ cm}^{-2}$ with a rotational temperature (T_{rot}) of 100.6 ± 30.4 K. The derive rotational temperature indicates that the emission lines of NH_2CN arise from the warm inner region of the G358.93–0.03 MM1 because the temperature of the hot molecular core is above 100 K (van Dishoeck & Blake 1998). The derived fractional abundance of NH_2CN with respect to H_2 towards the G358.93–0.03 MM1 was $(4.72 \pm 2.0) \times 10^{-10}$, where the H_2 column density was $(1.25 \pm 0.11) \times 10^{24} \text{ cm}^{-2}$.

4 Discussion

4.1 Comparison with other sources

Here we compare the observed abundance of NH_2CN in G358.93–0.03 MM1 and other hot molecular cores, galaxies, high and low-mass protostars, and molecular clouds, which are shown in Table 6. The estimated abundance of NH_2CN towards the G358.93–0.03 MM1 is $(4.72 \pm 2.0) \times 10^{-10}$. This means the abundance of NH_2CN towards the G358.93–0.03 MM1 is nearly similar to that of the sculptor galaxy NGC 253 and the low-mass protostars IRAS 16293–2422 B and NGC 1333 IRAS4A2. The abundance of NH_2CN towards G358.93–0.03 MM1 is approximately one order of magnitude higher as compared to the hot molecular cores Sgr B2(OH), Sgr B2(N), and Sgr B2(M), and the low-mass protostar NGC 1333 IRAS2A. Similarly, the abundance of NH_2CN towards G358.93–0.03 MM1 is approximately one order of magnitude lower as compared to the high-mass protostar IRAS 20126+4104 and the molecular cloud G+0.693. We also observed that the abundance of NH_2CN towards G358.93–0.03 MM1 is approximately two orders of magnitude lower as compared to the hot molecular core G10.47+0.03. This result indicates the formation route(s) of NH_2CN towards G358.93–0.03 MM1 is similar to NGC 253, IRAS 16293–2422 B, and NGC 1333 IRAS4A2.

4.2 Possible formation and destruction pathways of NH_2CN

In the hot core and corino objects, the formation mechanism of NH_2CN was poorly understood. According to the KIDA (Wakelam et al. 2012) astrochemistry molecular reactions database, there are no gas-phase reactions that produce the abundance of NH_2CN . We found two gas-phase reactions of NH_2CN in the UMIST 2012 (McElroy et al. 2013) astrochemistry chemical network database that have the ability to synthesise NH_2CN . According to the UMIST 2012 database, the NH_2CN molecule was created via the neutral-neutral reaction between NH_3 and CN ($\text{CN} + \text{NH}_3 \rightarrow \text{NH}_2\text{CN} + \text{H}$) and electron recombination of NH_2CNH^+ ($\text{NH}_2\text{CNH}^+ + e^- \rightarrow \text{NH}_2\text{CN} + \text{H}$). Earlier, Coutens et al. (2018) also proposed another pathway for the formation of NH_2CN via the neutral-neutral reaction between NH_2 and CN ($\text{NH}_2 + \text{CN} \rightarrow \text{NH}_2\text{CN}$). Earlier, Manna & Pal (2022a) claimed the neutral-neutral reaction between NH_3 and CN is responsible for the formation of NH_2CN towards the hot molecular core G10.47+0.03. The electron recombination of NH_2CNH^+ was assumed to create NH_2CN only in 5% of cases (Belloche et al. 2017). Earlier, Coutens et al. (2018) claimed the neutral-neutral reaction between NH_2 and CN is the most effective pathway to produce NH_2CN on the

Table 6 Column density and abundance of NH₂CN towards different types of sources.

Source name	Type	$N(\text{NH}_2\text{CN})$ (cm ⁻²)	Tex (K)	$N(\text{H}_2)$ (cm ⁻²)	Abundance	Reference
G358.93–0.03 MM1	Hot molecular core	$(5.90 \pm 2.5) \times 10^{14}$	100.6 \pm 30.4	$(1.25 \pm 0.11) \times 10^{24}$	$(4.72 \pm 2.0) \times 10^{-10}$	This work
G10.47+0.03	Hot molecular core	$(6.60 \pm 0.1) \times 10^{15}$	201.2 \pm 3.3	1.30×10^{23}	5.07×10^{-8}	Manna & Pal (2022a)
Sgr B2(OH)	Hot molecular core	2.0×10^{15}	15	5.0×10^{23}	4.0×10^{-11}	Cummins et al. (1986)
Sgr B2(N)	Hot molecular core	2.3×10^{14}	500	3.0×10^{24}	7.6×10^{-11}	Nummelin et al. (2000)
Sgr B2(M)	Hot molecular core	3.0×10^{13}	68	2.0×10^{24}	1.5×10^{-11}	Nummelin et al. (2000)
NGC 253	Sculptor Galaxy	1.2×10^{13}	67	6.5×10^{22}	2.0×10^{-10}	Martín et al. (2006)
IRAS 20126+4104	High-mass protostar	3.3×10^{15}	210	2.7×10^{24}	1.2×10^{-9}	Palau et al. (2017)
IRAS 16293–2422 B	Low-mass protostar	7.0×10^{13}	300	1.2×10^{25}	2.0×10^{-10}	Coutens et al. (2018)
NGC 1333 IRAS2A	Low-mass protostar	2.5×10^{14}	130	5.0×10^{24}	5.0×10^{-11}	Coutens et al. (2018)
NGC 1333 IRAS4A2	Low-mass protostar	8.5×10^{14}	150	5.0×10^{24}	1.7×10^{-10}	Belloche et al. (2020)
G+0.693	Giant molecular cloud	3.8×10^{13}	6.3	1.35×10^{23}	2.3×10^{-9}	Zeng et al. (2018)

grain surface of hot cores and corinos. Recently, Zhang et al. (2023) also claimed the neutral-neutral reaction between NH₂ and HNC is responsible for the formation of NH₂CN towards the hot corinos and hot molecular cores. Similarly, NH₂CN will be destroyed via photochemical reaction (NH₂CN + hν → NH₂ + CN), cosmic ray-induced photoreaction (NH₂CN + CRPHOT → NH₂ + CN), and ion-neutral reaction (H₃⁺ + NH₂CN → NH₂CNH⁺ + H₂) (McElroy et al. 2013). Recently, Zhang et al. (2023) also presented more destruction pathways of NH₂CN in Table 2 in the context of hot corinos and hot molecular cores.

4.3 Previous chemical modelling of NH₂CN in the hot molecular cores

To understand the formation mechanisms and abundance of NH₂CN towards hot molecular cores and hot corinos, Coutens et al. (2018) used the three-phase (gas + dust + ice) warm-up chemical model using the chemical kinetics code MAGICCAL (Garrod 2013). The chemical modelling of Coutens et al. (2018) is similar to the three-phase warm-up chemical model of Garrod (2013) which was applied towards the hot molecular cores. During the chemical modelling, Coutens et al. (2018) used both low-density (1.6×10^7 cm⁻³) and high-density (6.0×10^{10} cm⁻³) conditions. The high-density (6.0×10^{10} cm⁻³) model is reasonable towards the hot corinos objects (IRAS 16293–2422, NGC 1333 IRAS2A, etc.) because the gas density of the hot corinos varies between $\sim 10^9$ and $\sim 10^{10}$ cm⁻³ (Coutens et al. 2018). The low-density (1.6×10^7 cm⁻³) model is reasonable towards the hot molecular core objects (G10.47+0.03, G31.41+0.31, Sgr B2, Orion KL, etc.) because the gas density of the hot molecular core varies between $\sim 10^6$ to $\sim 10^8$ cm⁻³ (van Dishoeck & Blake 1998; Garrod 2013). During the chemical modelling of NH₂CN in low-density conditions, Coutens et al. (2018) used the neutral-neutral reaction between NH₂ and CN (NH₂ + CN → NH₂CN) in the grain/ice chemical network to estimate the abundance of NH₂CN. During the chemical modelling of NH₂CN in low-density conditions, Coutens et al. (2018) considered

an isothermal collapse phase followed by a static warm-up phase. In the first phase (the free-fall collapse stage), the gas density rapidly increased from $\sim 1.1 \times 10^3$ to 1.6×10^7 cm⁻³, while the dust temperature decreased from 16 K to 8 K. In the second phase (the warm-up stage), the density of gas was fixed at 1.6×10^7 cm⁻³ and the temperature of the dust fluctuated between 8 K and 400 K. After the modelling, Coutens et al. (2018) estimated that the abundance of NH₂CN was 3.7×10^{-10} in the case of the low-density model in the warm-up stage.

To ensure the chemical modelling of Coutens et al. (2018), we also examined another three-phase warm-up chemical modelling of NH₂CN created by Zhang et al. (2023). For chemical modelling of NH₂CN towards the hot molecular cores, Zhang et al. (2023) used the NAUTILUS chemical code, which includes the gas, dust surface, and icy mantle. In the first phase (the freefall collapse stage), Zhang et al. (2023) assumed the hot molecular cores undergoes the isothermal collapse phase at 10 K, and gas density rapidly increases from $n_H = 3 \times 10^3$ cm⁻³ to 1.6×10^7 cm⁻³. The first phase begins at $A_V = 2$ mag and progresses to more than 200 mag. In the second phase (the warm-up phase), the gas density is fixed at 1.6×10^7 cm⁻³, and the temperature increases from 10 K to 200 K over the time scale 4×10^5 yr. During the chemical modelling of NH₂CN, Zhang et al. (2023) used the reaction NH₂ + CN → NH₂CN in the grain surface to estimate the abundance of NH₂CN. In the warm-up phase, Zhang et al. (2023) observed that the abundance of NH₂CN varies between 2.0×10^{-10} to 6.0×10^{-9} .

4.4 Comparison between observed and modelled abundances of NH₂CN

To understand the formation pathways of NH₂CN towards G358.93–0.03 MM1, we compare our estimated observed abundance of NH₂CN with the modelled abundance of NH₂CN estimated by the low-density model of Coutens et al. (2018) and Zhang et al. (2023). This comparison is physically reasonable because the temperature and gas density of G358.93–0.03 MM1 are ~ 150 K (Chen et al. 2020) and

$\sim 2 \times 10^7 \text{ cm}^{-3}$ (Stecklum et al. 2021), respectively. Earlier, Coutens et al. (2018) showed that the modelled abundance of NH_2CN is 3.7×10^{-10} . Similarly, Zhang et al. (2023) observed the abundance of NH_2CN varies between 2.0×10^{-10} to 6.0×10^{-9} . We find that our estimated abundance of NH_2CN towards G358.93–0.03 MM1 is $(4.72 \pm 2.0) \times 10^{-10}$, which is very close to the range of the modelled abundance of NH_2CN in Coutens et al. (2018) and Zhang et al. (2023). This comparison indicates that NH_2CN molecule is created in the grain surfaces of G358.93–0.03 MM1 via the neutral-neutral reaction between NH_2 and CN ($\text{NH}_2 + \text{CN} \rightarrow \text{NH}_2\text{CN}$).

4.5 Searching of urea ($\text{NH}_2\text{C}(\text{O})\text{NH}_2$) towards the G358.93–0.03 MM1

After the detection of the possible urea ($\text{NH}_2\text{C}(\text{O})\text{NH}_2$) precursor molecule NH_2CN from the G358.93–0.03 MM1, we also attempted to search for the rotational emission lines of $\text{NH}_2\text{C}(\text{O})\text{NH}_2$ from the sub-millimeter spectra of the G358.93–0.03 MM1. After careful spectral analysis, we did not detect the emission lines of $\text{NH}_2\text{C}(\text{O})\text{NH}_2$ within the limits of our LTE spectral modelling. We estimated the upper limit column density of $\text{NH}_2\text{C}(\text{O})\text{NH}_2$ was $\leq (1.2 \pm 0.8) \times 10^{13} \text{ cm}^{-2}$. Furthermore, we calculated the upper limit of the $\text{NH}_2\text{C}(\text{O})\text{NH}_2$ and NH_2CN column density ratios towards the G358.93–0.03 MM1 as 0.020 ± 0.016 . For searching the emission lines of $\text{NH}_2\text{C}(\text{O})\text{NH}_2$, we used the Cologne Database for Molecular Spectroscopy (CDMS) spectroscopic molecular database (Müller et al. 2005). Our detection of the amide-like molecule NH_2CN towards the hot molecular core G358.93–0.03 MM1 using the ALMA gives more confidence that the G358.93–0.03 MM1 has the ability to create other amide-related molecules. We propose a spectral line survey of formamide (NH_2CHO), acetamide ($\text{CH}_3\text{C}(\text{O})\text{NH}_2$), and N-methyl formamide (CH_3NHCHO) with better spectral resolution and a higher integration time to solve the prebiotic chemistry of the amide-related molecules in the ISM.

5 Conclusion

We analysed the ALMA band 6 data of the high-mass star-formation region G358.93–0.03, and we extracted the molecular lines from the hot molecular core G358.93–0.03 MM1. The main conclusions of this work are as follows:

1. We identified a total of seven rotational emission lines of NH_2CN towards the hot molecular core G358.93–0.03 MM1 using the ALMA band 6 observations.
2. The estimated column density of NH_2CN towards the

G358.93–0.03 MM1 was $(5.9 \pm 2.5) \times 10^{14} \text{ cm}^{-2}$ with a rotational temperature of $100.6 \pm 30.4 \text{ K}$. The derived abundance of NH_2CN towards the G358.93–0.03 MM1 with respect to H_2 was $(4.72 \pm 2.0) \times 10^{-10}$.

3. We compared the estimated abundance of NH_2CN towards G358.93–0.03 MM1 with other sources. We observe the abundance of NH_2CN towards G358.93–0.03 MM1 is nearly similar to that of the sculptor galaxy NGC 253 and the low-mass protostars IRAS 16293–2422 B and NGC 1333 IRAS4A2. That means the formation route(s) of NH_2CN towards G358.93–0.03 MM1 are similar to NGC 253, IRAS 16293–2422 B, and NGC 1333 IRAS4A2.

4. We compared our estimated abundance of NH_2CN with the modelled abundances of NH_2CN , which was estimated by Coutens et al. (2018) and Zhang et al. (2023). After the comparison, we found that the observed abundance of NH_2CN is nearly similar to the modelled abundances of NH_2CN . This comparison indicates that the NH_2CN molecule was created in the grain surfaces of G358.93–0.03 MM1 via the neutral-neutral reaction between NH_2 and CN ($\text{NH}_2 + \text{CN} \rightarrow \text{NH}_2\text{CN}$).

5. After the identification of the NH_2CN towards the G358.93–0.03 MM1, we also looked for the emission lines of urea ($\text{NH}_2\text{C}(\text{O})\text{NH}_2$). After the spectral analysis, we did not detect the emission lines of $\text{NH}_2\text{C}(\text{O})\text{NH}_2$ within the limits of LTE analysis. We estimated the upper limit column density of $\text{NH}_2\text{C}(\text{O})\text{NH}_2$ as $\leq (1.2 \pm 0.8) \times 10^{13} \text{ cm}^{-2}$. We also derive the upper limit of the $\text{NH}_2\text{C}(\text{O})\text{NH}_2$ and NH_2CN column density ratios towards the G358.93–0.03 MM1 as 0.020 ± 0.016 . The unsuccessful detection of $\text{NH}_2\text{C}(\text{O})\text{NH}_2$ using the ALMA indicated that the emission lines of $\text{NH}_2\text{C}(\text{O})\text{NH}_2$ may be below the confusion limit towards the G358.93–0.03 MM1.

Acknowledgments

We thank the anonymous referee for the helpful comments that improved the manuscript. A.M. acknowledges the Swami Vivekananda Merit-cum-Means Scholarship (SVMCM) for financial support for this research. This paper makes use of the following ALMA data: ADS/JAO.ALMA#2019.1.00768.S. ALMA is a partnership of ESO (representing its member states), NSF (USA), and NINS (Japan), together with NRC (Canada), MOST and ASIAA (Taiwan), and KASI (Republic of Korea), in cooperation with the Republic of Chile. The Joint ALMA Observatory is operated by ESO, AUI/NRAO, and NAOJ.

Data availability

The data that support the plots within this paper and other findings of this study are available from the corresponding author upon reasonable request. The raw ALMA data are publicly available at <https://almascience.nao.ac.jp/asax/> (project id: 2019.1.00768.S).

Funding

No funds or grants were received during the preparation of this manuscript.

Conflicts of interest

The authors declare no conflict of interest.

Author Contributions

S.P. conceptualize the project. A.M. analysed the ALMA data and identify the emission lines of cyanamide (NH_2CN) from G358.93–0.03 MM1. A.M. analyses the rotational diagram to derive the column density and rotational temperature of NH_2CN . A.M. and S.P. wrote the main manuscript text. All authors reviewed the manuscript.

References

- Aladro, R., Martín, S., Martín-Pintado, J. et al. 2011, *A&A*, 535, A84
- Bayandina, O.S., Brogan, C.L., Burns, R.A., et al. 2022, *AJ*, 163(2), p.83
- Belloche, A., Meshcheryakov, A. A., Garrod, R. T., et al. 2017, *A&A*, 601, A49
- Belloche A. et al., 2020, *A&A* , 635, A198
- Brogan, C. L., Hunter, T. R., Towner, A. P. M., et al. 2019, *ApJL*, 881, L39
- Brown, R. D., Godfrey, P. D., Kleibömer, B., 1985, *Journal of Molecular Spectroscopy*, 2, 257-273
- Chen, X., Sobolev, A. M., Ren, Z.-Y., et al. 2020, *NatAs*, 4, 1170
- Coutens, A., Willis, E. R., Garrod, R. T., et al. 2018, *A&A*, 612, A107
- Comrie, A., Wang, K.-S., Ford, P., et al. 2021, CARTA: The Cube Analysis and Rendering Tool for Astronomy, 1.3.0, Zenodo
- Cummins S. E., Linke R. A., Thaddeus P., 1986, *ApJS* , 60, 819
- Duvernay, F., Chiavassa, T., Borget, F., & Aycard, J.-P. 2005, *J. Phys. Chem. A*, 109, 603
- Garrod, R. T., & Herbst, E. 2006, *A&A*, 457, 927
- Garrod, R. T. 2013, *ApJ*, 765, 60
- Goldsmith, P. F., & Langer, W. D. 1999, *ApJ*, 517, 209
- Gorai, P., Das, A., Shimonishi, T., et al. 2021, *ApJ*, 907, 108
- Jiménez-Serra, I., Martín-Pintado, J., Rivilla, V. M., Rodríguez-Almeida, L., Alonso, A. E. R., Zeng, S., Cocinero, E. J., Martín, S., Requena-Torres, M., Martín-Domenech, R., Testi, L., 2020, *Astrobiology*, 20, 9, 1048-1066
- Kilpatrick, M. L. 1947, *J. Am. Chem. Soc.*, 69, 40
- Ligterink, N. F. W., El-Abd, S. J., Brogan, C. L., et al. 2020, *ApJ*, 901, 37
- Manna, A. & Pal, S., 2022, *Journal of Astrophysics and Astronomy*, 43, 83
- Manna, A. & Pal, S., 2022, *Life Sciences in Space Research*, 34, 9
- Martín S., Mauersberger R., Martín-Pintado J., Henkel C., García-Burillo S., 2006, *ApJS* , 164, 450
- Müller, H. S. P., SchilMöder, F., Stutzki, J. & Winnewisser, G. 2005, *Journal of Molecular Structure*, 742, 215–227
- McElroy, D., Walsh, C., Markwick, A. J., Cordiner, M. A., Smith, K., Millar, T. J., 2013, *A&A*, 550, A36
- McMullin, J. P., Waters, B., Schiebel, D., et al. 2007, San Francisco, CA: ASP, 127
- Motogi, K., Hirota, T., Machida, M. N., et al. 2019, *ApJL*, 877, L25
- Mangum, J., 2020, How to Calculate Bandwidth Smearing in Radio Synthesis Measurements, NRAO
- Nummelin A., Bergman P., Hjalmarson Å., Friberg P., Irvine W. M., Millar T. J., Ohishi M., Saito S., 2000, *ApJS* , 128, 213
- Cox, A. N., & Pilachowski, C. A. 2000, *Physics Today*, 53, 77
- Pickett, H. M., Poynter, R. L., Cohen, E. A., et al. 1998, *Journal of Quantitative Spectroscopy and Radiative Transfer*, 60, 883
- Palau, A., Walsh, C., Sánchez-Monge, Á., Girart, J. M., Cesaroni, R., Jiménez-Serra, I., Fuente, A., Zapata, L. A., Neri, R., 2017, *MNRAS*, 467, 2723
- Perley, R. A., Butler, B. J. 2017, *ApJ*, 230, 1538
- Reid, M. J., Menten, K. M., Brunthaler, A., et al. 2014, *ApJ*, 783, 130
- Shimonishi, T., Izumi, N., Furuya, K., & Yasui, C., 2021, *ApJ*, 2, 206
- Sharma, M. K., *Astrophysics*, 2021, 64,71-80
- Stecklum, B., Wolf, V., Linz, H., et al., 2021. *A&A*, 646, p.A161
- Turner, B. E., Liszt, H. S., Kaifu, N., & Kisliakov, A. G. 1975, *ApJ*, 201, L149
- van Dishoeck E. F., & Blake G. A. 1998, *Annu Rev Astron Astrophys*, 36, 317
- Vastel, C., Bottinelli, S., Caux, E., et al. 2015, *Proceedings of the Annual meeting of the French Society of Astronomy and Astrophysics*, 313-316
- Williams, A., & Ibrahim, I. T. 1981, *Chem. Rev.*, 81, 589
- White, G. J., Araki, M., Greaves, J. S., Ohishi, M., & Higginbottom, N. S. 2003, *A&A*, 407, 589
- Whittet, D. C. B. 1992, *Journal of the British Astronomical Association*, 102, 230
- Wakelam V., et al., 2012, *The Astrophysical Journal Supplement*, 199, 21
- Zeng S. et al., 2018, *MNRAS* , 478, 2962
- Zhang, X., et al., 2023, *MNRAS*, 521, 1578